Three-Dimensional Numerical Modeling of Coseismic Atmospheric Dynamics and Ionospheric Responses in Slant Total Electron Content Observations

P.A. Inchin[1,2], Y. Kaneko[3], A.-A. Gabriel[4,5], T. Ulrich[5], L. Martire[6], A. Komjathy[6], J. Aguilar Guerrero[1], M.D. Zettergren[1], J.B. Snively[1]

[1]Center for Space and Atmospheric Research, Embry-Riddle Aeronautical University, Daytona Beach, Florida, USA
[2]Computational Physics, Inc., Springfield, Virginia 22151, USA
[3]Department of Geophysics, Kyoto University, Kyoto, Japan
[4]Scripps Institution of Oceanography, University of California San Diego, La Jolla, CA, USA
[5]Department of Earth and Environmental Sciences, Ludwig-Maximilians-University, Munich, Germany
[6]Jet Propulsion Laboratory, California Institute of Technology, Pasadena, California, USA

Key Points:

- Acoustic-gravity wave-driven slant total electron content (sTEC) signals are analyzed in terms of amplitude, waveform, and onset time
- Intricate sTEC signal waveforms result from ionospheric fluctuations measured along lines-of-sight between satellites and receivers
- High sensitivity of sTEC signals to acoustic-gravity wave source specification provides additional basis for earthquake characterization

Corresponding author: P.A. Inchin, pinchin@cpi.com

Abstract

Despite routine detection of coseismic acoustic-gravity waves (AGWs) in Global Navigation Satellite System (GNSS) total electron content (TEC) observations, models of the earthquake-atmosphere-ionosphere dynamics, essential for validating data-driven studies, remain limited. We present the results of three-dimensional numerical simulations encompassing the entire coupling from Earth's interior to the ionosphere during the M_w 7.8 2016 Kaikoura earthquake. Incorporating the impact of data/model uncertainties in estimating the ionospheric state, the results show a good agreement between observed and simulated slant TEC (sTEC) signals, assessed through a set of metrics. The signals exhibit intricate waveforms, resulting from the integrated nature of TEC and phase cancellation effects, emphasizing the significance of direct signal comparisons along realistic line-of-sight paths. By conducting simulations based on earthquake representations with kinematic and dynamic source models, the study demonstrates the quantifiable sensitivity of sTEC to AGW source specifications, pointing to their utility in the analysis of coupled dynamics.

Plain Language Summary

Earthquakes launch acoustic and acoustic-gravity waves (AGWs) into the atmosphere, spanning periods from seconds to minutes, that can reach the ionosphere at ∼100-400 km altitude. The majority of AGW detections in the ionosphere are performed with the use of GNSS signals collected with ground-based receivers that nowadays comprehensively cover seismically active regions. However, the modeling of earthquake-atmosphere-ionosphere processes together, essential for validating and supporting data-driven studies, remains rare. We present the outcomes of three-dimensional numerical modeling of interconnected processes, spanning from Earth's interior to the ionosphere. We conducted a case study focused on the 2016 M_w 7.8 earthquake in New Zealand, renowned for its complexity and comprehensive observations of coseismic AGWs recorded with GNSS signals. Our results demonstrate a high level of accuracy of simulated GNSS signals, also revealing the high sensitivity to the chosen earthquake model and the complexity of resulting ionospheric signals, highlighting the necessity of attributing realistic geometries of GNSS TEC observations. The findings highlight the potential for using GNSS signals to investigate coseismic AGWs to infer characteristics of earthquakes.

1 Introduction

Seismically-excited acoustic-gravity waves (AGWs) in the atmosphere serve as sources of detectable ionospheric plasma density fluctuations (Hines, 1960; Blanc, 1985; Tanaka et al., 1984; Ducic et al., 2003). They are routinely detected by measuring delays of Global Navigation Satellite System (GNSS) signals to infer fluctuations in total electron content (TEC), which is directly proportional to the integrated number of electrons along the path between a GNSS satellite and a ground-based receiver (e.g., Parkinson et al., 1995). The distribution of GNSS receivers in seismically active regions and advancements in temporal resolution of measurements, have significantly bolstered the use of TEC for the detection and analysis of coseismic AGWs (Occhipinti et al., 2013; Komjathy et al., 2016; Astafyeva, 2019). The studies rely on the temporal and spatial characteristic variability of TEC signals, including arrival times (Astafyeva & Shults, 2019; Thomas et al., 2018; Sanchez et al., 2023), amplitudes (Cahyadi & Heki, 2014; Manta et al., 2020; Inchin et al., 2021), and shapes (Astafyeva & Heki, 2009a; Bagiya et al., 2023; Brissaud & Astafyeva, 2022), showing promise for enhancing the operational capabilities of systems that monitor AGW fluctuations in the ionosphere (Savastano et al., 2017; Ravanelli et al., 2021; Maletckii & Astafyeva, 2021; Manta et al., 2021; Martire et al., 2023). Under the introduced terminology AGW, we include infrasonic (acoustic) waves, which, in addition to propagating by compressional motions of air, are also influenced by buoyant stratification of the atmosphere at periods close to acoustic cut-off frequency.

At the same time, simulations of earthquake-atmosphere-ionosphere processes, essential for validating data-driven studies, remain challenging. Firstly, the development of comprehensive earthquake source models is essential and necessitates a thorough consideration of the rupture process to address resulting atmospheric dynamics (Astafyeva & Heki, 2009b; Bagiya et al., 2018). Secondly, high-resolution three-dimensional nonlinear and compressible atmospheric models are required for simulating AGWs with periods ranging from seconds to minutes (Inchin, Snively, Williamson, et al., 2020). The resolution of AGWs is required over comparatively large regions to cover line-of-sights (LOS) between GNSS satellites and ground-based receivers. Thirdly, the direct modeling of ionospheric responses to AGWs is also crucial, taking into account potential nonlinear behavior and the complexity of plasma responses to neutral gas drivers within ambient geomagnetic field (Zettergren & Snively, 2015, 2019). Atmospheric and ionospheric simulations must effectively account for background states and winds, which influence AGW propagation and resulting plasma drifts (Drob et al., 2003; McDonald et al., 2012). The scope and complexity of these processes necessitate a comprehensive analysis of the dynamics at every step and in every system.

The magnitude 7.8 Kaikoura earthquake struck the South Island of New Zealand on November 13, 2016 T_0=11:02:56 UT (11/14/2016, 00:02:56 local time) and resulted in more than 20 fault segments ruptured, including some previously unknown or considered inactive. Despite the availability of various geophysical datasets, the complete understanding of its rupture evolution remains elusive, positioning this earthquake as one of the most intricate records to date (Kaiser et al., 2017; Hamling et al., 2017). Despite this, the ionospheric responses to coseismic AGWs were measured by a substantial number of multi-GNSS receivers across New Zealand. These detections offered an opportunity to investigate and quantify coseismic processes for an inland earthquake together with ionosphere responses and to propose new techniques for earthquake source characterization (Bagiya et al., 2018; Lee et al., 2018; Zedek et al., 2021; Inchin et al., 2021).

We report new results leveraging our fully-3D modeling approach for simulating earthquake-atmosphere-ionosphere coupling processes, applied to the M_w 7.8 Kaikoura earthquake and its associated sTEC signals. We investigate the structure of electron density fluctuations along LOS and the resulting sTEC signals and assess the impacts of uncertainties in estimating background ionospheric states on them. In addition to simulations utilizing the earthquake's kinematic source model, we here compare to simulations with a multi-fault dynamic rupture earthquake source model.

2 Methodology

We conducted seismic wave propagation simulations with the specification of kinematic and dynamic earthquake source models. The first corresponds to the kinematic source model of Inchin et al. (2021), constrained by strong-motion, InSAR, Global Positioning System (GPS), vertical coastal uplift and tsunami data, and was used to initialize a SPECFEM3D simulation (Komatitsch & Vilotte, 1998; Komatitsch & Tromp, 2002). For the second, coupled dynamic source model and wave propagation simulation was conducted with the SeisSol software (Dumbser & Käser, 2006; Pelties et al., 2013; Breuer et al., 2014; Uphoff et al., 2017) with dynamic source model described in Ulrich et al. (2019). Coupling with nonlinear and compressible neutral atmosphere model MAGIC3D was made through the transfer of vertical momentum at the surface (Inchin, Snively, Zettergren, et al., 2020). MAGIC3D simulations were configured with a spatial resolution of 500 m in horizontal and 250 m in vertical directions. Atmospheric stratification and winds were based on global empirical models NRLMSISE-00 and HWM-14 (Picone et al., 2002;

Drob et al., 2015), and covered the heights from the surface to 500 km, with $\sim$9×17.7° in meridional and zonal directions. Geomagnetic indexes Kp and Dst during the events were 3 and -20 nT, respectively. The output of the MAGIC3D simulations, including perturbations in major gas species densities, temperature, and fluid velocities, served as drivers in the three-dimensional ionospheric model GEMINI3D. The basis for MAGIC3D and GEMINI3D are described in Zettergren and Snively (2015).

GNSS TEC observations were calculated using software developed at the Jet Propulsion Laboratory gnsstec.py (JPL New Technology Report #52034, Bertiger et al. (2020)) and GIM (Mannucci et al., 1998). We utilized raw GPS and GLONASS navigation and observation data at a sampling rate of 1 Hz in Receiver Independent Exchange Format (RINEX). For observations, the height of 300 km was specified as ionospheric shell layer to calculate ionospheric pierce point (IPP) positions and the absolute vTEC was estimated using a Single Layer Mapping function. Model synthesized sTEC signals were calculated from the integration of electron densities (n_e), based on the outputs of n_e from GEMINI3D simulations. To compare measured and simulated sTEC signals along temporally and spatially varying LOS, we applied a Butterworth filter with a fourth-order and a window of 30-600 sec. To obtain simulated n_e perturbation fields, we performed GEMINI3D simulation excluding AGWs, and subtracted fields of n_e from AGW-driven run.

3 Results

3.1 Ionospheric responses to coseismic AGWs

The results of seismic wave propagation simulations with a kinematic source model and atmospheric dynamics were presented by Inchin et al. (2021), whereas here we focus on fully-3D ionospheric plasma responses to AGWs and sTEC signals. During the local night-time of the event, the absolute vTEC exhibited values ranging between 6-14 TEC units (TECu) across New Zealand (Figure 1c). While a broad positive gradient of vTEC is evident from south to north, the observations reveal intricate variations in vTEC, potentially attributable to ionospheric disturbances of diverse origins. To address the uncertainty in estimation of absolute vTEC, expected to be at the level ± several TECu (Ren et al., 2019; Wielgosz et al., 2021; Chen et al., 2020), and its role in determining AGW signals in sTEC ($\sim$0.02-0.2 TECu), we conducted two GEMINI3D simulations corresponding to the background ionospheric conditions at the time of the earthquake T_0 and T_0-30 min, but with the same seismic wave propagation and AGW simulation inputs with kinematic source model, referred to as Sim #1 and Sim #2. Figure 1a,b depicts the absolute vTEC from these simulations. Simulated vTEC ranges from $\sim$5-7 TECu at the south to $\sim$11-14 TECu over the Northern Island, giving difference between the simulations of 2-5 TECu over the numerical domain. Figure 1d,e illustrate n_e fields from Sim #1 along the meridional and zonal directions with altitudes, respectively, sliced over the center of GEMINI3D domain. The electron density peak altitude (hmF2) from simulations is at $\sim$300 km, reaching values of 5.5×10^{11} m^{-3}.

Figure 2a-d illustrate the snapshots of simulated sTEC fluctuations, assuming zenith-looking LOSs. The leading fluctuations, surpassing the typical noise level of TEC at $\sim$0.01-0.02 TECu, become discernible $\sim$10 min after T_0. The time required for the rupture propagation spans over $\sim$90 sec, with the most pronounced AGWs being generated $\sim$60-80 sec after the rupture initiation (Inchin et al., 2021). The leading fluctuations are slightly inclined towards the northeast, aligning with the direction of rupture propagation. They arise from n_e perturbations occurring at altitudes of $\sim$230-250 km, revealing plasma drifts not fully aligned with magnetic field lines and influenced by larger neutral-ion collision frequency at these altitudes. The strongest sTEC fluctuations, in this LOS geometry, are simulated over the Cook Strait, with the positive phase reaching the area $\sim$12 min after T_0. The dominant following plasma drifts are primarily aligned with magnetic field lines and evolve equatorward (Figure 2c,d).

Figure 2e,f display maximum sTEC fluctuations (in LOS geometry as in panels a-d) and neutral major gas temperature perturbations (their moduli) at 300 km altitude. The strongest AGWs are found to the north and northeast from the epicenter, arising from the northeastward propagation of the rupture and focusing of AGWs. Concurrently, the strongest sTEC fluctuations, up to 0.26 TECu, are observed over the Cook Strait. The fluctuations to the west and south from the epicenter, as well as offshore to the east, also exhibit amplitudes higher than TEC noise level, in the range of ∼0.02-0.08 TECu. The disparities between the fields of simulated sTEC signals and AGW-driven fluctuations highlight the significance of the alignment of plasma drifts driven by AGWs with magnetic field, exhibiting dominant equatorward motion, even in the present of large amplitude dynamics in the neutral gas (Rolland et al., 2013; Zettergren & Snively, 2015; Bagiya et al., 2017).

Simulated n_e fluctuations for six satellite-station pairs along their actual LOSs with time are presented in top panels of Figure 2g-l. Their Y axes are altitudes along LOSs. In the corresponding bottom panels, we show the resultant sTEC signals (black lines) and the altitude at which n_e fluctuations contribute the most to sTEC signals (red lines). The onset time of sTEC signals corresponds to altitudes ∼230-260 km, depending on the elevation angle and positioning of LOS. This suggests that sTEC signals are sensitive to AGW-driven fluctuations at altitudes significantly lower than hmF2. The complexity of n_e fluctuations along the LOS demonstrates the fact that they, and thus sTEC signals, do not originate from a single, fixed altitude. Instead, this altitude varies in accordance with the evolving plasma drifts over time. While the initial fluctuations in sTEC may arise from n_e fluctuations contributing at lower altitudes, the peak amplitudes of these signals can result from heights close to hmF2 or higher at 400-500 km.

The nature of sTEC, which involves integrating n_e along the LOS, can introduce complexities that lead to the potential cancellation of otherwise detectable fluctuations. This is demonstrated in Figure 2i,l, where the initial positive-phase fluctuations (top panels), although present, contribute minimally to the resulting sTEC signals (bottom panels). Subsequent negative-phase fluctuations dominate in contribution to sTEC, ultimately resulting in an initial negative phase in signals. The phase-cancellation effect may lead to signals falling below the threshold of detectability, as demonstrated for the GPS51-HANM pair. This behavior of n_e fluctuations implies apparent delayed detectability of sTEC when observed with unsuitable LOS. Likewise, the period and shape of these signals vary depending the alignment of plasma drifts relative to the LOS.

3.2 Comparison of observed and synthetic sTEC signals

Figure 3 provides a comparison between observed and simulated sTEC signals. The focus of our analysis lies within observations taken over Cook Strait. The other groups of observations originated from areas west of the epicenter, spanning over North Island of New Zealand, and over the ocean to the east of the epicenter. Although still finding a sufficient level of agreement with observations, we omitted most signals originating to the south of South Island, as they consistently exhibited signal amplitudes below expected TEC noise level (∼0.01-0.02 TECu). Simulated sTEC signals in Figure 3 are calculated along actual LOSs, i.e., in the same geometry as they were observed during the event.

First, we find that the variability of the background ionospheric state between Sim #1 and Sim #2 does not translate into a notable difference in simulated sTEC signals and neither of the simulations outperformed when compared with the observations. We expect that the presented uncertainty associated with absolute vTEC may not necessarily be a source of error when simulating sTEC signals driven by AGWs. However, we expect that larger discrepancies in absolute vTEC or variations in the ionospheric layering unrelated to the event may lead to more significant differences in simulated sTEC fluctuations.

The highest level of agreement of simulated and observed sTEC signals is over Cook Strait with a similar level of concordance to the west and northwest of the epicenter. A common trend of smaller amplitudes in the simulated signals over Northern Island is noted. Here, despite closely matching the shapes of the signals and onset times, simulated sTEC consistently exhibit ∼50% lower amplitudes. It is unlikely that the underestimation of absolute vTEC is the primary cause of such differences. This discrepancy may be due to the inaccuracies of 3D velocity structure, especially in the offshore region, assumed in the earthquake model or under-resolving related AGW dynamics in the atmosphere. Separately, analyzing sTEC signals to the east of the epicenter, we find that their amplitudes are effectively captured by simulations, but they appear ∼20 sec earlier in time than the observed ones. We attribute this to a potential lack of constraints on rupture propagation offshore, which is less evident based on available geodetic data. Lastly, Figure 3 presents a comparison of signals located to the south of the epicenter, which mostly agree, but exhibit limited utility due to low signal-to-noise ratio. Understanding the causes of sTEC discrepancies for some satellite-station pairs to the north and east require further in-depth parametric investigation.

To quantify the differences between simulated and observed sTEC, we implemented a set of metrics, including the time of flight (TOF), maximum and minimum amplitudes, the duration of pulses, and the temporal track cross-correlation of signals. An example of metrics estimation is presented for pair GPS51-LEVN in Figure 3 and full metric analysis is provided in the Supplemental Materials. The TOF error is determined as the difference between the observed and simulated sTEC fluctuation onset times. As the onset time, we identify the point at which the derivative of the sTEC signal exceeds the trend four times. The errors in amplitude and the duration are calculated for the main pulse, which falls between signal onset time and the point where the N-shaped pulse crosses zero amplitude from negative. The cross-correlation coefficient, providing a measure of observed and synthetic signal linear dependence, is calculated over a period from 120 sec before the TOE to the last simulated time step. The selected subset of 92 satellite-station pairs is focused on clearly identifiable signals of AGWs in sTEC, where metrics could be calculated automatically. The underesolved signals to the north of the North Island, east to the Ocean and south (with sTEC signals close or below the TEC noise of ∼0.01-0.02 TECu) are excluded from the analysis.

On average, the metric errors are as follows: ∼15 sec for TOF, 10.4% for the duration of the pulse, and 12.2% for the temporal track cross-correlation of signals and 17.9% for the maximum and 20.2% for the minimum amplitudes of the pulse. We find relatively small error in the TOF constituting ∼15 sec. This error is significantly smaller than the time of AGW arrival from the ground of 600 sec, on average (i.e., $Onset_{obs} - T_0$ sec, where $Onset_{obs}$ is observed sTEC fluctuation onset time), implying sufficiently accurate timing of the source model and good estimation of atmospheric speeds of sound and ionospheric fluctuation altitudes relative to layers. Similarly, we find favorable agreement for the temporal cross-correlation of signals and the period of pulses. The error in pulse duration, ∼30 sec, is relatively small compared to the total period of the signals, which ranges from ∼300-480 sec, implying reasonable constraint on the source spectrum as well as timing considerations. We find higher levels of errors in the amplitudes of simulated fluctuations, which are found to be the most challenging to replicate, but note that these errors (∼0.01-0.04 TECu) are close to the noise level of TEC observations themselves.

3.3 Kinematic vs dynamic earthquake source model

We performed a set of simulations using the 3D dynamic rupture (e.g, Harris et al., 2018) earthquake source model proposed by Ulrich et al. (2019), referenced as Sim

#3 below. The advantage of dynamic source modeling compared to kinematic models is to account for the physics of spontaneous rupture nucleation, propagation and arrest, which, while more complex, can help to address the problems of non-uniqueness of solutions based on purely data-driven source inversion techniques (e.g., Taufiqurrahman et al., 2023; Jia et al., 2023). Thus, the dynamic model, although less-tuned to describe the observations, serves as a tool for understanding the physics underlying rupture progression, which is especially important for complex earthquakes. Additionally, the ruptured faults and the segment sequence in dynamic model by Ulrich et al. (2019) differs from the kinematic source model by Inchin et al. (2021). The background state of the ionosphere in Sim #3 is specified from Sim #1.

Figure 4a,b illustrates the comparison of maximum absolute vertical velocities at the Earth surface from Sim #1 and Sim #3. The amplitudes are higher in Sim #3 than those simulated with kinematic source model (Sim #1), varying to 3 times in some areas. Related to Sim #3 simulation revealed that AGW amplitudes reach values of 369 m/s of the leading shock and -760 m/s of the tail shock of N-wave at 300 km altitude, exceeding the values from Sim #1 to ∼90%. For comparison, Figure 4c demonstrates Sim #3 maximum temperature perturbations at 300 km altitude, which peak at 321 K and are ∼50% larger than in Sim #1.

Although Sim #3 results in stronger AGWs in the atmosphere than Sim #1, the possibility to infer these differences based on sTEC is yet not clear. Thus, Figure 4d shows sTEC signals from Sim #3 compared with sTEC observations and results of Sim #1. We find markedly stronger sTEC fluctuations in Sim #3, exceeding the amplitudes of observed signals to ∼70-100%. A common earlier onset times of signals of ∼40-50 sec is also evident in Sim #3. This points to the importance of a nonlinear evolution of AGWs to acoustic shock N-waves with height, which then lengthen and exhibit speeds of its leading shock fronts faster than local speed of sound. Likewise, the steepness of the signal is more pronounced in Sim #3 than found in observations or in Sim #1, highlighting the nonlinear evolution of AGWs. Such disagreements between observed and simulated signals is found for practically all sTEC signals (additional figures are provided in the SM) in this case. Thus, the dynamic source model would require additional ingredients to fully capture surface vertical motions (e.g., Kaneko & Goto, 2022; Schliwa & Gabriel, 2024), potentially including GNSS TEC signals of coseismic AGWs as novel constraints.

4 Discussion and Conclusion

We presented the results of novel 3D direct numerical simulations, encompassing the chain of dynamics extending from Earth's interior and surface, to the atmosphere and to the ionosphere in response to the 2016 M_w 7.8 Kaikoura earthquake. They have enabled us to conduct a comparison between observed and simulated GNSS sTEC signals, considering variations in LOS paths and thus delving into the intricacies of sTEC signals. Our findings highlight that sTEC signal shapes provide a direct representation of the evolution of AGWs even though the structure of the signals is significantly influenced by the integration of electron density fluctuations along the LOS. The geometric phase-cancellation effect can result in the attenuation of AGW-driven fluctuations in sTEC signals below the detectability threshold, making it challenging to accurately determine signal onset times just relying on data. The results also suggest dominant sTEC signal components originating from different altitudes, above or below the peak of electron density. This questions the common practice of using a fixed IPP height to localize sTEC fluctuations, which are particularly relevant in the context of GNSS TEC observations with low elevation angles, when estimated IPP positions change rapidly. The findings highlight that direct comparisons of simulated and observed sTEC signals along realistic LOS can reduce ambiguity and improve fidelity.

The results demonstrated a high level of agreement between observed and simulated sTEC signals utilizing a kinematic source model, reinforcing the appropriateness of this simulation approach and model specifications for constraining surface motion that drives AGWs. The set of metrics shows promise for applications in the analysis of other seismic events. At the same time, simulations initialized with the dynamic source model find sTEC signal differences reflecting the presence of higher vertical velocities (than simulated with kinematic slip model) at the Earth's surface that act as sources of AGWs. This further highlights the opportunity to employ sTEC signals for constraining surface dynamics during seismic events and to enhance earthquake source models and their validation. Results reinforce the importance of using a large number of observations for the analysis and validation of observational and simulation results, making sTEC particularly attractive to investigate spatially resolved AGW signals in the ionosphere that provide insight into their source geometries and evolutions.

Open Research

The SPECFEM3D software is preserved at `https://geodynamics.org/resources/specfem3dcartesian`, available via the GPL 3 license. The open-source software SeisSol is publicly available: `https://github.com/SeisSol/SeisSol` with BSD 3-Clause Licence. GEMINI3D model is available through `https://github.com/gemini3d/gemini3d` (Zettergren & Hirsch, 2024) with Apache-2.0 license. GNSS TEC observations used for the investigation of travelling ionospheric disturbances in the study are available at GeoNet Aotearoa New Zealand Continuous GNSS Network AWS Open Data access mechanism `https://www.geonet.org.nz/data/access/aws` with public access.

Conflict of Interest Statement

The authors declare no conflicts of interest relevant to this study.

Acknowledgements

This research is supported by NASA ESI 80NSSC22K0507 and 80NSSC20K0495, DARPA Cooperative Agreement HR00112120003, and JSPS KAKENHI (21H05206). This work is approved for public release; distribution is unlimited. The content of the information does not necessarily reflect the position or the policy of the Government, and no official endorsement should be inferred. Part of this research was carried out at the Jet Propulsion Laboratory, California Institute of Technology, under a contract with NASA 80NM0018D0004. A.-A.G. and T.U. acknowledge support by the European Union's Horizon 2020 research and innovation programme (grant no. 852992), Horizon Europe (grant nos. 101093038, 101058129, 101058518), and NSF (grant nos. EAR-2225286, EAR-2121568, OAC-2139536, OAC-2311208).

References

Astafyeva, E. (2019). Ionospheric detection of natural hazards. *Reviews of Geophysics*, *57*(4), 1265-1288. doi: 10.1029/2019RG000668

Astafyeva, E., & Heki, K. (2009a). Dependence of waveform of near-field coseismic ionospheric disturbances on focal mechanisms. *Earth Planets Space*, *61*(7), 939–943. doi: 10.1186/BF03353206

Astafyeva, E., & Heki, K. (2009b). Dependence of waveform of near-field coseismic ionospheric disturbances on focal mechanisms. *Earth, Planets and Space*, *61*, 939–943. doi: 10.1186/BF03353206

Astafyeva, E., & Shults, K. (2019). Ionospheric gnss imagery of seismic source: Possibilities, difficulties, and challenges. *Journal of Geophysical Research: Space Physics*, *124*(1), 534-543. doi: 10.1029/2018JA026107

Bagiya, M. S., Heki, K., & Gahalaut, V. K. (2023). Anisotropy of the near-field coseismic ionospheric perturbation amplitudes reflecting the source process: The 2023 february turkey earthquakes. *Geophysical Research Letters*, *50*(14), e2023GL103931. doi: https://doi.org/10.1029/2023GL103931

Bagiya, M. S., Sunil, A. S., Sunil, P. S., Sreejith, K. M., Rolland, L., & Ramesh, D. S. (2017). Efficiency of coseismic ionospheric perturbations in identifying crustal deformation pattern: Case study based on mw 7.3 may nepal 2015 earthquake. *Journal of Geophysical Research: Space Physics*, *122*(6), 6849-6857. doi: 10.1002/2017JA024050

Bagiya, M. S., Sunil, P. S., Sunil, A. S., & Ramesh, D. S. (2018). Coseismic Contortion and Coupled Nocturnal Ionospheric Perturbations During 2016 Kaikoura, Mw 7.8 New Zealand Earthquake. *J. Geophys. Res.: Space Physics*, *123*(2), 1477-1487. doi: 10.1002/2017JA024584

Bertiger, W., Bar-Sever, Y., Dorsey, A., Haines, B., Harvey, N., Hemberger, D., ... others (2020). Gipsyx/rtgx, a new tool set for space geodetic operations and research. *Advances in space research*, *66*(3), 469–489.

Blanc, E. (1985). Observations in the upper atmosphere of infrasonic waves from natural or artificial sources: a summary. *Annales Geophysicae*, *3*, 673–687.

Breuer, A., Heinecke, A., Rettenberger, S., Bader, M., Gabriel, A.-A., & Pelties, C. (2014). Sustained petascale performance of seismic simulations with seissol on supermuc. In *Supercomputing: 29th international conference, isc 2014, leipzig, germany, june 22-26, 2014. proceedings 29* (pp. 1–18).

Brissaud, Q., & Astafyeva, E. (2022, 05). Near-real-time detection of co-seismic ionospheric disturbances using machine learning. *Geophysical Journal International*, *230*(3), 2117-2130. doi: 10.1093/gji/ggac167

Cahyadi, M. N., & Heki, K. (2014, 11). Coseismic ionospheric disturbance of the large strike-slip earthquakes in North Sumatra in 2012: Mw dependence of the disturbance amplitudes. *Geophysical Journal International*, *200*(1), 116-129. doi: 10.1093/gji/ggu343

Chen, P., Liu, H., Ma, Y., & Zheng, N. (2020). Accuracy and consistency of different global ionospheric maps released by igs ionosphere associate analysis centers. *Advances in Space Research*, *65*(1), 163–174.

Drob, D. P., Emmert, J. T., Meriwether, J. W., Makela, J. J., Doornbos, E., Conde, M., ... Klenzing, J. H. (2015). An update to the Horizontal Wind Model (HWM): The quiet time thermosphere. *Earth and Space Science*, *2*(7), 301-319. doi: 10.1002/2014EA000089

Drob, D. P., Picone, J. M., & Garcés, M. (2003). Global morphology of infrasound propagation. *Journal of Geophysical Research: Atmospheres*, *108*(D21). doi: 10.1029/2002JD003307

Ducic, V., Artru, J., & Lognonné, P. (2003). Ionospheric remote sensing of the Denali Earthquake Rayleigh surface waves. *Geophys. Res. Lett.*, *30*(18). doi: 10.1029/2003GL017812

Dumbser, M., & Käser, M. (2006, 10). An arbitrary high-order discontinuous Galerkin method for elastic waves on unstructured meshes — II. The three-dimensional isotropic case. *Geophysical Journal International*, *167*(1), 319-336. doi: 10.1111/j.1365-246X.2006.03120.x

Hamling, I. J., Hreinsdóttir, S., Clark, K., Elliott, J., Liang, C., Fielding, E., ... Stirling, M. (2017). Complex multifault rupture during the 2016 Mw 7.8 Kaikoura earthquake, New Zealand. *Science*, *356*(6334). doi: 10.1126/science.aam7194

Harris, R. A., Barall, M., Aagaard, B., Ma, S., Roten, D., Olsen, K., ... others (2018). A suite of exercises for verifying dynamic earthquake rupture codes. *Seismological Research Letters*, *89*(3), 1146–1162.

Hines, C. O. (1960). Internal atmospheric gravity waves at ionospheric heights. *Canadian Journal of Physics*, *38*(11), 1441–1481.

Inchin, P., Snively, J., Kaneko, Y., Zettergren, M., & Komjathy, A. (2021). Inferring the evolution of a large earthquake from its acoustic impacts on the ionosphere. *AGU Advances*, *2*(2), e2020AV000260. doi: 10.1029/2020AV000260

Inchin, P., Snively, J., Williamson, A., Melgar, D., Aguilar Guerrero, J., & Zettergren, M. (2020). Mesopause airglow disturbances driven by nonlinear infrasonic acoustic waves generated by large earthquakes. *Journal of Geophysical Research: Space Physics*, e2019JA027628. doi: 10.1029/2019JA027628

Inchin, P., Snively, J., Zettergren, M., Komjathy, A., Verkhoglyadova, O., & Tulasi Ram, S. (2020). Modeling of Ionospheric Responses to Atmospheric Acoustic and Gravity Waves Driven by the 2015 Nepal 7.8 Gorkha Earthquake. *Journal of Geophysical Research: Space Physics*, *125*(4), e2019JA027200. doi: 10.1029/2019JA027200

Jia, Z., Jin, Z., Marchandon, M., Ulrich, T., Gabriel, A.-A., Fan, W., ... others (2023). The complex dynamics of the 2023 kahramanmaraş, turkey, m w 7.8-7.7 earthquake doublet. *Science*, *381*(6661), 985–990.

Kaiser, A., Balfour, N., Fry, B., Holden, C., Litchfield, N., Gerstenberger, M., ... others (2017). The 2016 kaikōura, new zealand, earthquake: preliminary seismological report. *Seismological Research Letters*, *88*(3), 727–739.

Kaneko, Y., & Goto, H. (2022). The origin of large, long-period near-fault ground velocities during surface-breaking strike-slip earthquakes. *Geophysical Research Letters*, *49*(10), e2022GL098029.

Komatitsch, D., & Tromp, J. (2002). Spectral-element simulations of global seismic wave propagation—ii. three-dimensional models, oceans, rotation and self-gravitation. *Geophys. J. Int.*, *150*(1), 303-318. doi: 10.1046/j.1365-246X.2002.01716.x

Komatitsch, D., & Vilotte, J.-P. (1998, 04). The spectral element method: An efficient tool to simulate the seismic response of 2D and 3D geological structures. *Bulletin of the Seismological Society of America*, *88*(2), 368-392.

Komjathy, A., Yang, Y.-M., Meng, X., Verkhoglyadova, O., Mannucci, A. J., & Langley, R. B. (2016). Review and perspectives: Understanding natural-hazards-generated ionospheric perturbations using gps measurements and coupled modeling. *Radio Sci.*, *51*(7), 951-961. doi: 10.1002/2015RS005910

Lee, R. F., Rolland, L. M., & Mikesell, D. T. (2018). Seismo-ionospheric observations, modeling, and backprojection of the 2016 Kaikōura earthquake. *Bulletin of the Seismological Society of America*, *108*(3B), 1794–1806. doi: 10.1785/0120170299

Maletckii, B., & Astafyeva, E. (2021). Determining spatio-temporal characteristics of coseismic travelling ionospheric disturbances (ctid) in near real-time. *Scientific Reports*, *11*(1), 20783.

Mannucci, A. J., Wilson, B. D., Yuan, D. N., Ho, C. H., Lindqwister, U. J., & Runge, T. F. (1998). A global mapping technique for gps-derived ionospheric total electron content measurements. *Radio Science*, *33*(3), 565-582. doi: 10.1029/97RS02707

Manta, F., Occhipinti, G., Feng, L., & Hill, E. M. (2020). Rapid identification of tsunamigenic earthquakes using gnss ionospheric sounding. *Scientific Reports*, *10*(1), 1–10.

Manta, F., Occhipinti, G., Hill, E. M., Perttu, A., Assink, J., & Taisne, B. (2021). Correlation between gnss-tec and eruption magnitude supports the use of ionospheric sensing to complement volcanic hazard assessment. *Journal of Geophysical Research: Solid Earth*, *126*(2), e2020JB020726.

Martire, L., Krishnamoorthy, S., Vergados, P., Romans, L. J., Szilágyi, B., Meng, X., ... Bar-Sever, Y. E. (2023). The GUARDIAN system-a GNSS upper atmospheric real-time disaster information and alert network. *GPS solutions*, *27*(1), 1–13.

McDonald, S. E., Drob, D. P., Emmert, J., Englert, C., Siskind, D., Huba, J., ...

Basu, S. (2012). The importance of thermospheric winds for ionospheric modeling. *A White Paper for the Decadal Survey of Solar and Space Physics*.

Occhipinti, G., Rolland, L., Lognonné, P., & Watada, S. (2013). From Sumatra 2004 to Tohoku-Oki 2011: The systematic GPS detection of the ionospheric signature induced by tsunamigenic earthquakes. *J. Geophys. Res.: Space Physics*, *118*(6), 3626-3636. doi: 10.1002/jgra.50322

Parkinson, B., Spilker, J., Axelrad, P., & Enge, P. (1995). Global positioning system: Theory and applications. *ISBN:1-56347-107-8*, *Volume I*.

Pelties, C., Gabriel, A., & Ampuero, J. (2013). Verification of an ader-dg method for complex dynamic rupture problems. *Geoscientific Model Development Discussion*, *6*, 5981–6034.

Picone, J., Hedin, A. E., Drob, D. P., & Aikin, A. C. (2002). NRLMSISE-00 empirical model of the atmosphere: Statistical comparisons and scientific issues. *J. Geophys. Res.*, *107*(A12), SIA 15-1-SIA 15-16. doi: 10.1029/2002JA009430

Ravanelli, M., Occhipinti, G., Savastano, G., Komjathy, A., Shume, E. B., & Crespi, M. (2021). Gnss total variometric approach: first demonstration of a tool for real-time tsunami genesis estimation. *Scientific Reports*, *11*(1), 3114.

Ren, X., Chen, J., Li, X., Zhang, X., & Freeshah, M. (2019). Performance evaluation of real-time global ionospheric maps provided by different igs analysis centers. *GPS Solutions*, *23*, 1–17.

Rolland, L. M., Vergnolle, M., Nocquet, J.-M., Sladen, A., Dessa, J.-X., Tavakoli, F., ... Cappa, F. (2013). Discriminating the tectonic and non-tectonic contributions in the ionospheric signature of the 2011, mw7.1, dip-slip van earthquake, eastern turkey. *Geophysical Research Letters*, *40*(11), 2518-2522. doi: 10.1002/grl.50544

Sanchez, S. A., Kherani, E. A., Astafyeva, E., & de Paula, E. R. (2023). Rapid detection of co-seismic ionospheric disturbances associated with the 2015 illapel, the 2014 iquique and the 2011 sanriku-oki earthquakes. *Journal of Geophysical Research: Space Physics*, *128*(9), e2022JA031231. doi: 10.1029/2022JA031231

Savastano, G., Komjathy, A., Verkhoglyadova, O., Mazzoni, A., Crespi, M., Wei, Y., & Mannucci, A. J. (2017). Real-time detection of tsunami ionospheric disturbances with a stand-alone gnss receiver: A preliminary feasibility demonstration. *Nature*, *7*.

Schliwa, N., & Gabriel, A.-A. (2024). Equivalent near-field corner frequency analysis of 3d dynamic rupture simulations reveals dynamic source effects. *Seismological Research Letters*, *95*(2A), 900–924.

Tanaka, T., Ichinose, T., Okuzawa, T., Shibata, T., Sato, Y., Nagasawa, C., & Ogawa, T. (1984). Hf-doppler observations of acoustic waves excited by the urakawa-oki earthquake on 21 march 1982. *Journal of Atmospheric and Terrestrial Physics*, *46*(3), 233-245. doi: 10.1016/0021-9169(84)90150-8

Taufiqurrahman, T., Gabriel, A.-A., Li, D., Ulrich, T., Li, B., Carena, S., ... Gallovič, F. (2023). Dynamics, interactions and delays of the 2019 ridgecrest rupture sequence. *Nature*, *618*(7964), 308–315.

Thomas, D., Bagiya, M. S., Sunil, P. S., Rolland, L., Sunil, A. S., Mikesell, T. D., ... Ramesh, D. S. (2018). Revelation of early detection of co-seismic ionospheric perturbations in GPS-TEC from realistic modelling approach: Case study. *Scientific Reports*, *8*, 2045-2322. doi: 10.1038/s41598-018-30476-9

Ulrich, T., Gabriel, A.-A., Ampuero, J.-P., & Xu, W. (2019). Dynamic viability of the 2016 Mw 7.8 Kaikōura earthquake cascade on weak crustal faults. *Nature Communications*, *10*(1), 1213. doi: 10.1038/s41467-019-09125-w

Uphoff, C., Rettenberger, S., Bader, M., Madden, E. H., Ulrich, T., Wollherr, S., & Gabriel, A.-A. (2017). Extreme scale multi-physics simulations of the tsunamigenic 2004 sumatra megathrust earthquake. Association for Computing Machinery. Retrieved from `https://doi.org/10.1145/3126908.3126948` doi: 10.1145/3126908.3126948

Wielgosz, P., Milanowska, B., Krypiak-Gregorczyk, A., & Jarmołowski, W. (2021). Validation of gnss-derived global ionosphere maps for different solar activity levels: Case studies for years 2014 and 2018. *GPS Solutions*, *25*(3), 103.

Zedek, F., Rolland, L. M., Mikesell, T. D., Sladen, A., Delouis, B., Twardzik, C., & Coïsson, P. (2021). Locating surface deformation induced by earthquakes using GPS, GLONASS and Galileo ionospheric sounding from a single station. *Advances in Space Research*, *68*(8), 3403–3416.

Zettergren, M., & Hirsch, M. (2024). *Gemini3D.* [Software]. Zenodo. doi: 10.5281/zenodo.10475267

Zettergren, M., & Snively, J. (2015). Ionospheric response to infrasonic-acoustic waves generated by natural hazard events. *J. Geophys. Res.*, *120*(9), 8002-8024. doi: 10.1002/2015JA021116

Zettergren, M., & Snively, J. (2019). Latitude and longitude dependence of ionospheric tec and magnetic perturbations from infrasonic-acoustic waves generated by strong seismic events. *Geophys. Res. Lett.*, *46*(3), 1132-1140. doi: 10.1029/2018GL081569

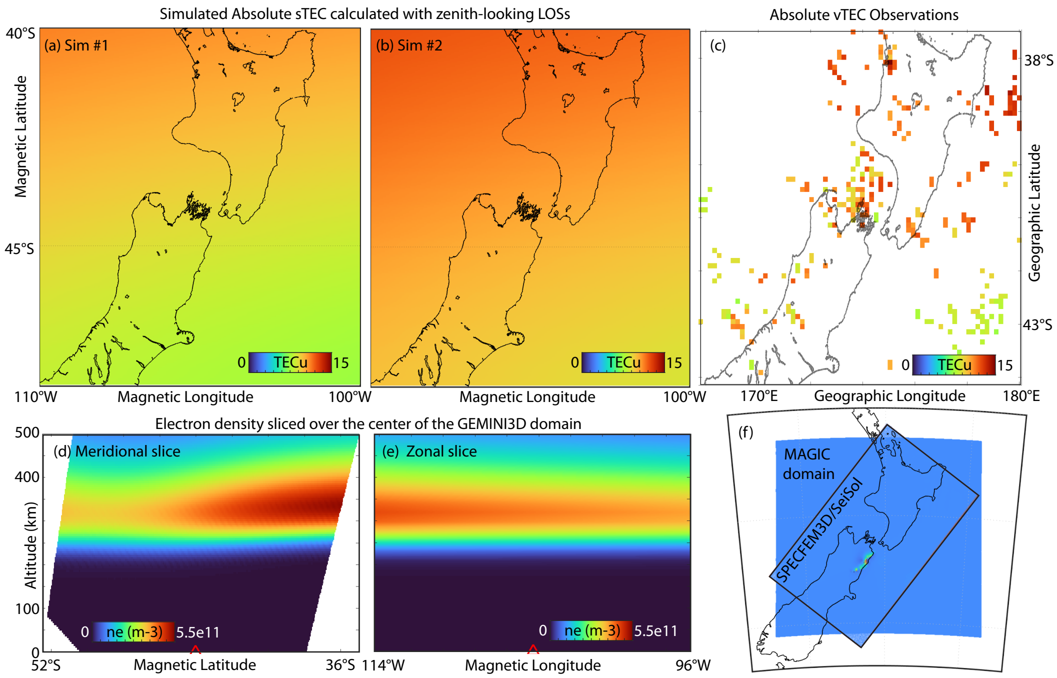

Figure 1. Absolute simulated sTEC calculated with zenith-looking LOSs at (a) 11:02:56 UT (Sim #1) and (b) 10:32:56 UT (Sim #2). (c) Observations of absolute vTEC at 11:00 UT. (d,e) Meridional and zonal slices of simulated electron density at 11:02:56 UT. (f) Schematic representation of maximum vertical velocities at the surface relative to the MAGIC3D numerical domains.

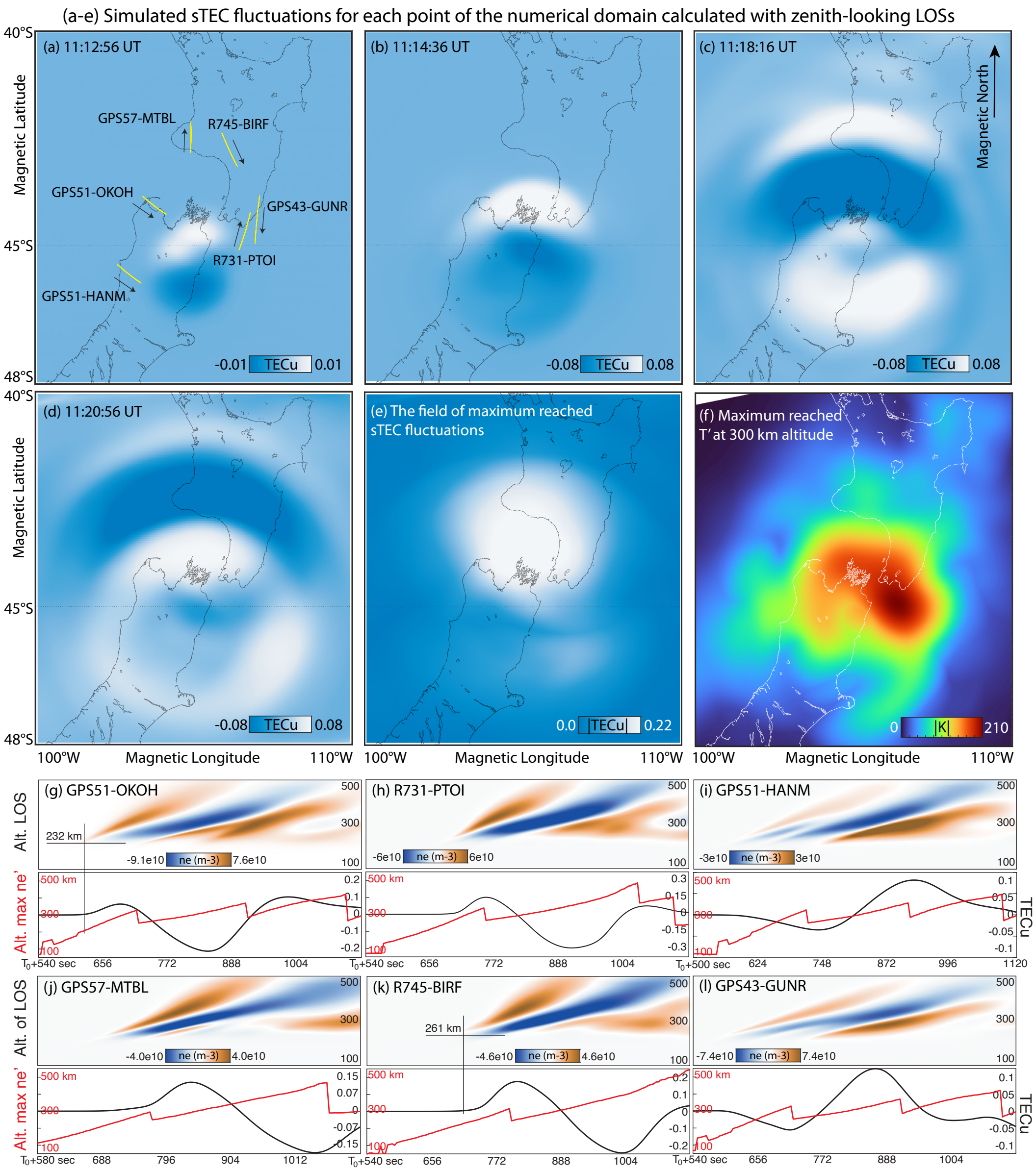

Figure 2. (a-d) The snapshots of simulated sTEC fluctuations calculated for each point of the numerical domain with zenith-looking LOSs at four epochs and (e) the field of their maximum values (moduli) calculated over the whole time of simulation. (f) Maximum neutral major gas temperature perturbations (moduli) at 300 km altitude calcualted over the whole time of simulatio. (g-l) Electron density (n_e) fluctuations over the time along realistically spatially and temporally varying LOSs and resulting sTEC signals (black lines) and the altitudes of maximum n_e fluctuations (red lines). The IPP positions for satellite-station pairs in panels g-l are shown in panel a with yellow lines for 20 min from T_0.

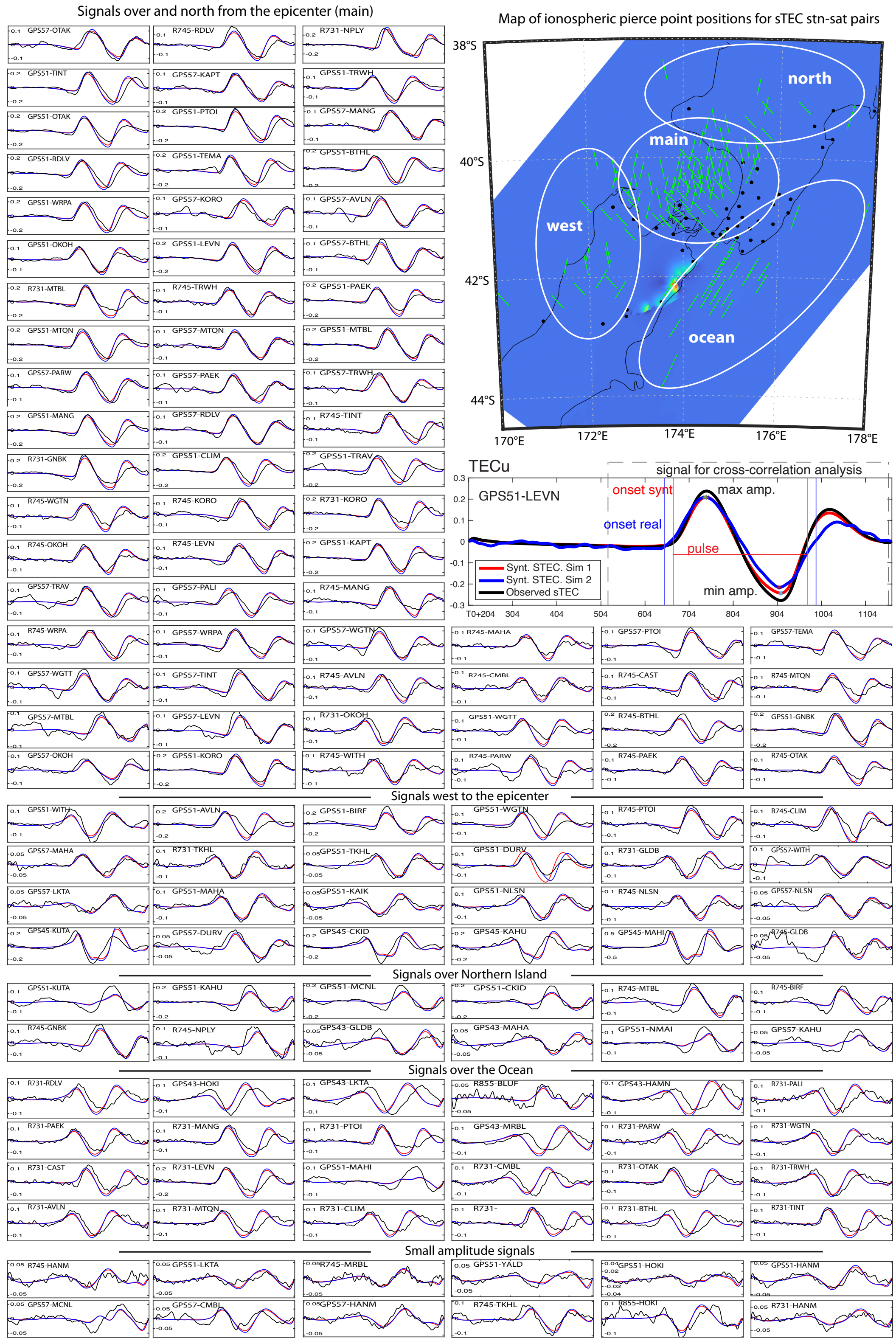

Figure 3. The comparison of observed (black lines) and simulated sTEC signals from Sim #1 (red lines) and Sim #2 (blue lines). Simulated sTEC signals are calculated along temporally and spatially varying LOSs, as measured during the event. Metrics analysis is presented for pair GPS51-LEVN. The time window from T_0+204 to T_0+1164 sec is chosen for all sTEC time series demonstrated. The map demonstrates IPP positions of observations. The elongated southwest-northeast rectangle illustrates final vertical displacements from Sim #1.

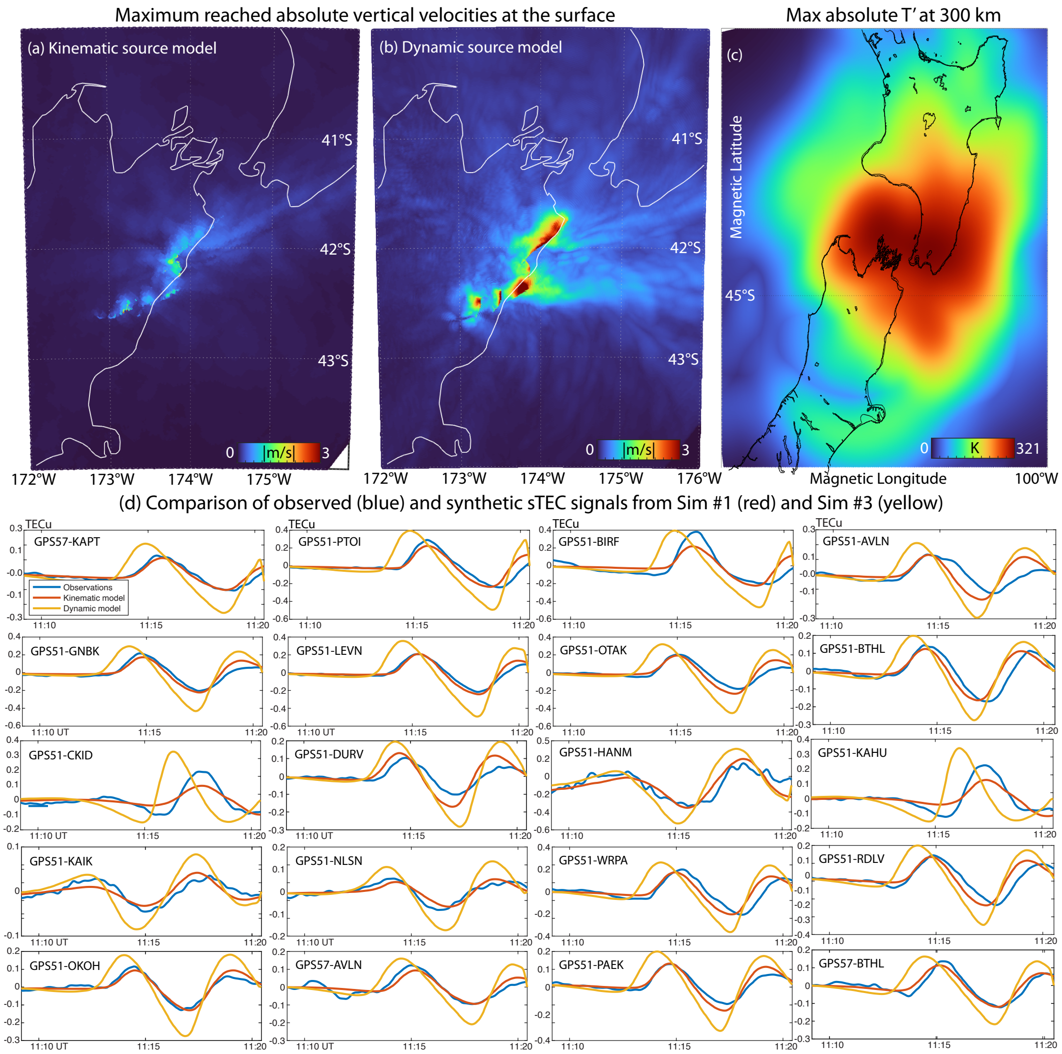

Figure 4. Maximum vertical velocities reached at the Earth's surface calculated based on the (a) kinematic source model (Sim #1) and (b) dynamic source model (Sim #2). (c) Maximum absolute temperature perturbations at 300 km altitude from simulation with dynamic source model. (d) Comparison of sTEC signals as observed (blue lines), derived from Sim #1 (red lines) and Sim #3 (yellow lines).

Figure 1.

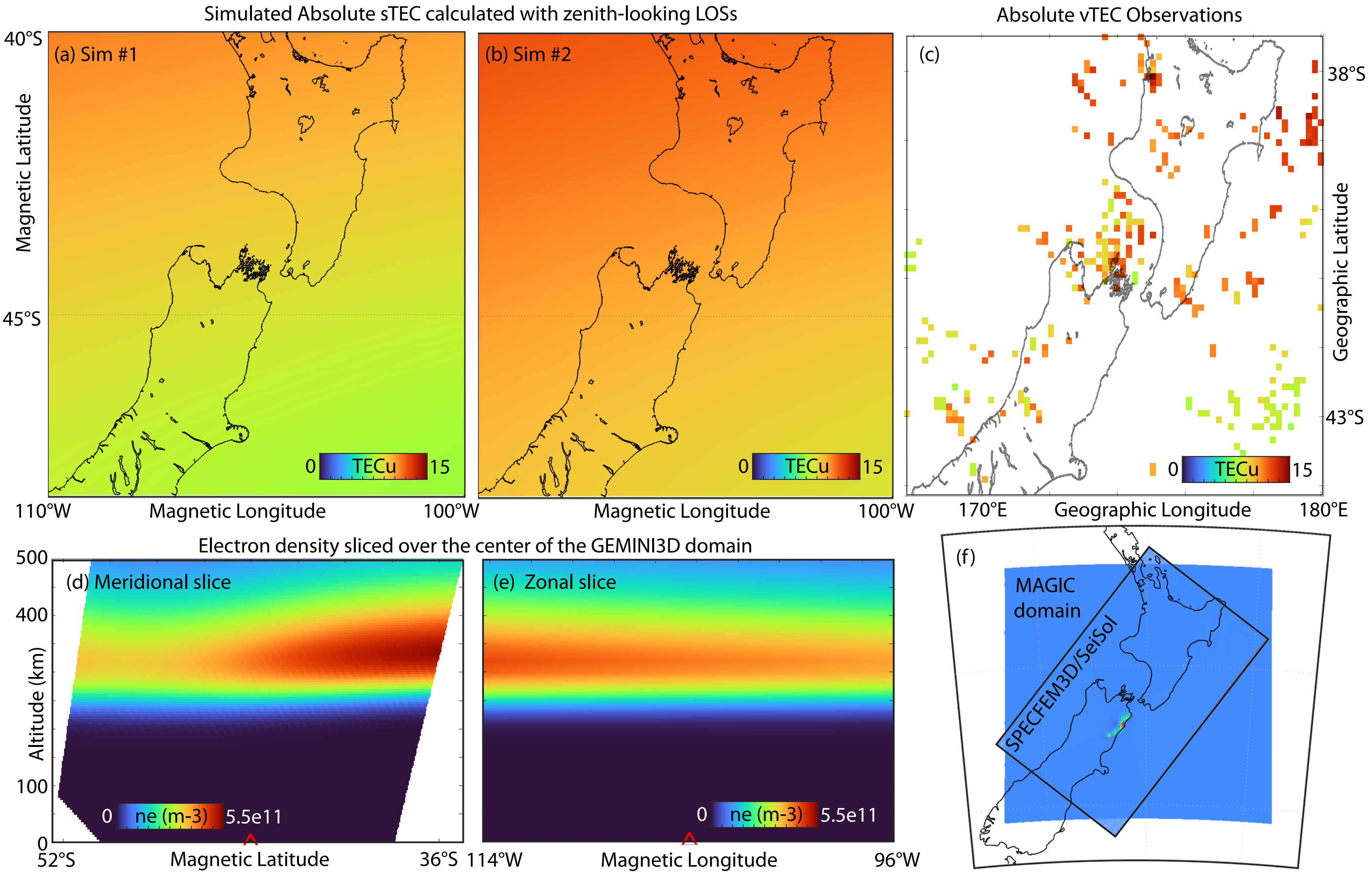

Simulated Absolute sTEC calculated with zenith-looking LOSs
(a) Sim #1
(b) Sim #2
40°S
45°S
Magnetic Latitude
0
TECu
15
110°W
Magnetic Longitude
100°W
Absolute vTEC Observations
(c)
38°S
43°S
Geographic Latitude
170°E
Geographic Longitude
180°E
Electron density sliced over the center of the GEMINI3D domain
(d) Meridional slice
(e) Zonal slice
500
400
100
0
Altitude (km)
ne (m-3)
5.5e11
52°S
Magnetic Latitude
36°S
114°W
Magnetic Longitude
96°W
(f)
MAGIC domain
SPECFEM3D/SeiSol

Figure 2.

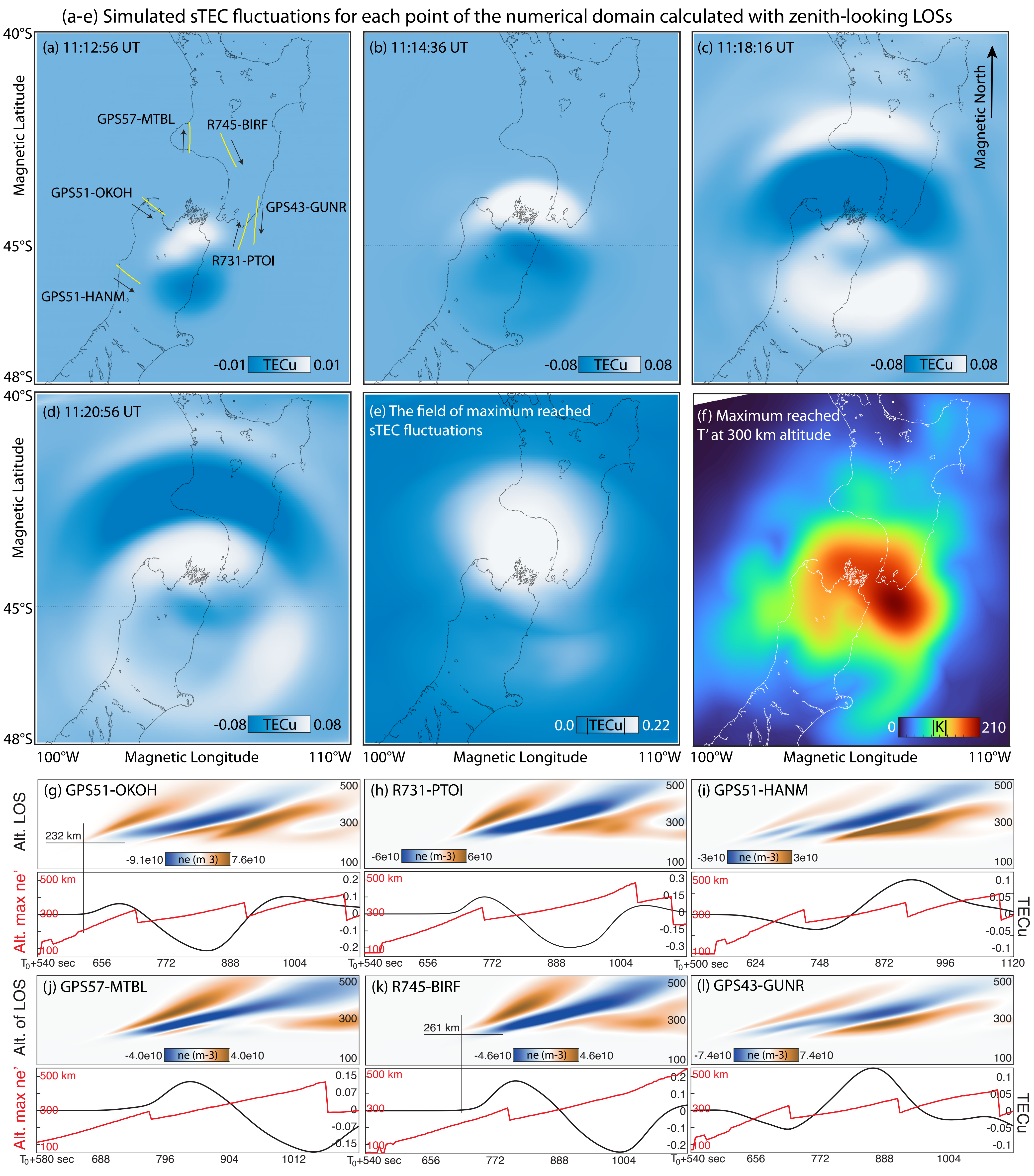

(a-e) Simulated sTEC fluctuations for each point of the numerical domain calculated with zenith-looking LOSs
(a) 11:12:56 UT
(b) 11:14:36 UT
(c) 11:18:16 UT
(d) 11:20:56 UT
(e) The field of maximum reached sTEC fluctuations
(f) Maximum reached T' at 300 km altitude
Magnetic North
Magnetic Latitude
Magnetic Longitude
40°S
45°S
48°S
100°W
110°W
GPS57-MTBL
R745-BIRF
GPS51-OKOH
GPS43-GUNR
R731-PTOI
GPS51-HANM
-0.01 TECu 0.01
-0.08 TECu 0.08
0.0 |TECu| 0.22
0 |K| 210
(g) GPS51-OKOH
(h) R731-PTOI
(i) GPS51-HANM
(j) GPS57-MTBL
(k) R745-BIRF
(l) GPS43-GUNR
Alt. LOS
Alt. of LOS
Alt. max ne'
232 km
261 km
-9.1e10 ne (m-3) 7.6e10
-6e10 ne (m-3) 6e10
-3e10 ne (m-3) 3e10
-4.0e10 ne (m-3) 4.0e10
-4.6e10 ne (m-3) 4.6e10
-7.4e10 ne (m-3) 7.4e10
500 km
TECu
T0+540 sec
T0+500 sec
T0+580 sec

Figure 3.

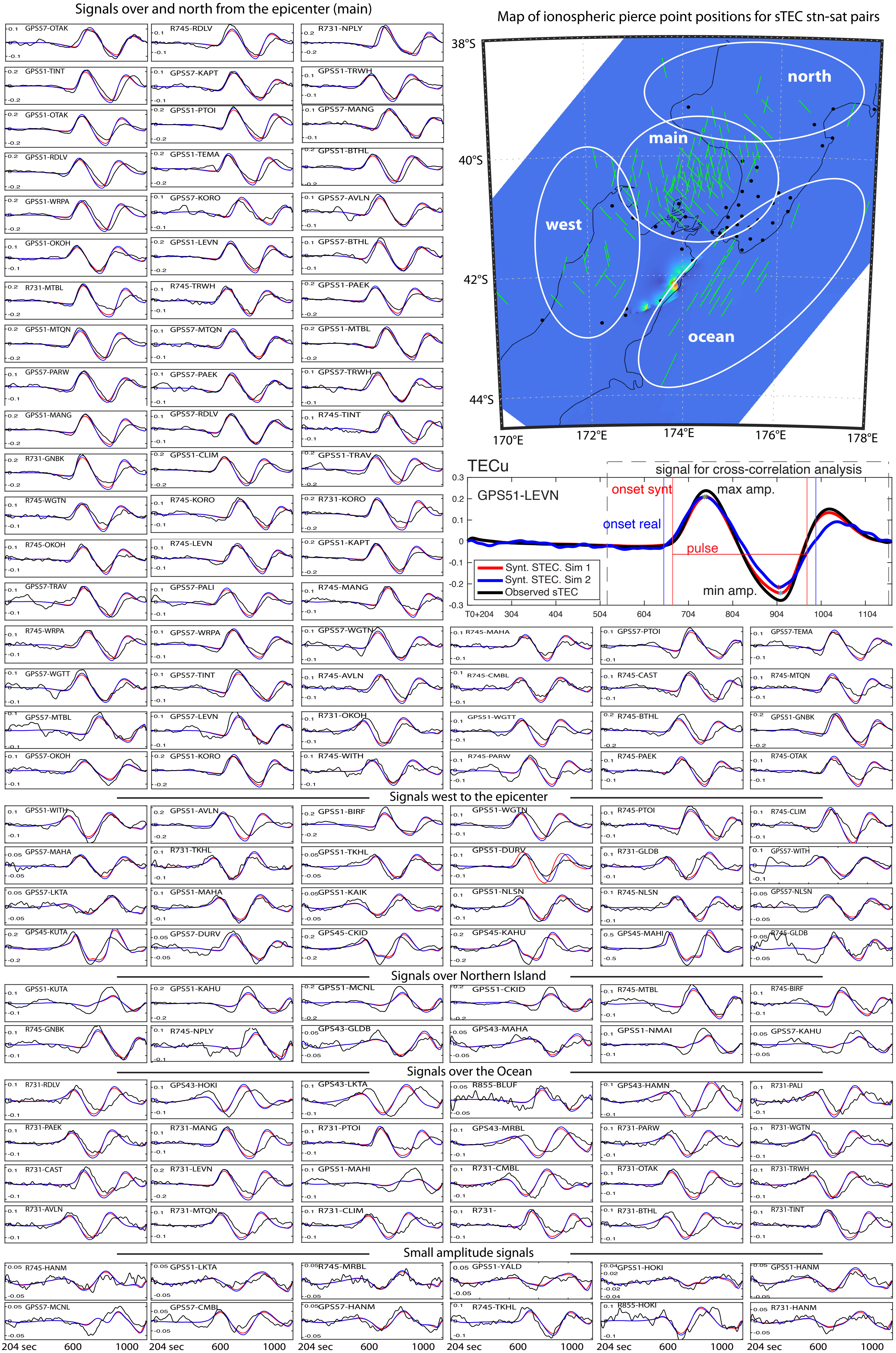

Signals over and north from the epicenter (main)
GPS57-OTAK
R745-RDLV
R731-NPLY
GPS51-TINT
GPS57-KAPT
GPS51-TRWH
GPS51-OTAK
GPS51-PTOI
GPS57-MANG
GPS51-RDLV
GPS51-TEMA
GPS51-BTHL
GPS51-WRPA
GPS57-KORO
GPS57-AVLN
GPS51-OKOH
GPS51-LEVN
GPS57-BTHL
R731-MTBL
R745-TRWH
GPS51-PAEK
GPS51-MTQN
GPS57-MTQN
GPS51-MTBL
GPS57-PARW
GPS57-PAEK
GPS57-TRWH
GPS51-MANG
GPS57-RDLV
R745-TINT
R731-GNBK
GPS51-CLIM
GPS51-TRAV
R745-WGTN
R745-KORO
R731-KORO
R745-OKOH
R745-LEVN
GPS51-KAPT
GPS57-TRAV
GPS57-PALI
R745-MANG
R745-WRPA
GPS57-WRPA
GPS57-WGTN
R745-MAHA
GPS57-PTOI
GPS57-TEMA
GPS57-WGTT
GPS57-TINT
R745-AVLN
R745-CMBL
R745-CAST
R745-MTQN
GPS57-MTBL
GPS57-LEVN
R731-OKOH
GPS51-WGTT
R745-BTHL
GPS51-GNBK
GPS57-OKOH
GPS51-KORO
R745-WITH
R745-PARW
R745-PAEK
R745-OTAK
Map of ionospheric pierce point positions for sTEC stn-sat pairs
38°S
40°S
42°S
44°S
170°E
172°E
174°E
176°E
178°E
north
main
west
ocean
TECu
signal for cross-correlation analysis
GPS51-LEVN
onset synt
max amp.
onset real
pulse
min amp.
Synt. STEC. Sim 1
Synt. STEC. Sim 2
Observed sTEC
T0+204
304
404
504
604
704
804
904
1004
1104
Signals west to the epicenter
GPS51-WITH
GPS51-AVLN
GPS51-BIRF
GPS51-WGTN
R745-PTOI
R745-CLIM
GPS57-MAHA
R731-TKHL
GPS51-TKHL
GPS51-DURV
R731-GLDB
GPS57-WITH
GPS57-LKTA
GPS51-MAHA
GPS51-KAIK
GPS51-NLSN
R745-NLSN
GPS57-NLSN
GPS45-KUTA
GPS57-DURV
GPS45-CKID
GPS45-KAHU
GPS45-MAHI
R745-GLDB
Signals over Northern Island
GPS51-KUTA
GPS51-KAHU
GPS51-MCNL
GPS51-CKID
R745-MTBL
R745-BIRF
R745-GNBK
R745-NPLY
GPS43-GLDB
GPS43-MAHA
GPS51-NMAI
GPS57-KAHU
Signals over the Ocean
R731-RDLV
GPS43-HOKI
GPS43-LKTA
R855-BLUF
GPS43-HAMN
R731-PALI
R731-PAEK
R731-MANG
R731-PTOI
GPS43-MRBL
R731-PARW
R731-WGTN
R731-CAST
R731-LEVN
GPS51-MAHI
R731-CMBL
R731-OTAK
R731-TRWH
R731-AVLN
R731-MTQN
R731-CLIM
R731-
R731-BTHL
R731-TINT
Small amplitude signals
R745-HANM
GPS51-LKTA
R745-MRBL
GPS51-YALD
GPS51-HOKI
GPS51-HANM
GPS57-MCNL
GPS57-CMBL
GPS57-HANM
R745-TKHL
R855-HOKI
R731-HANM
204 sec
600
1000

Figure 4.

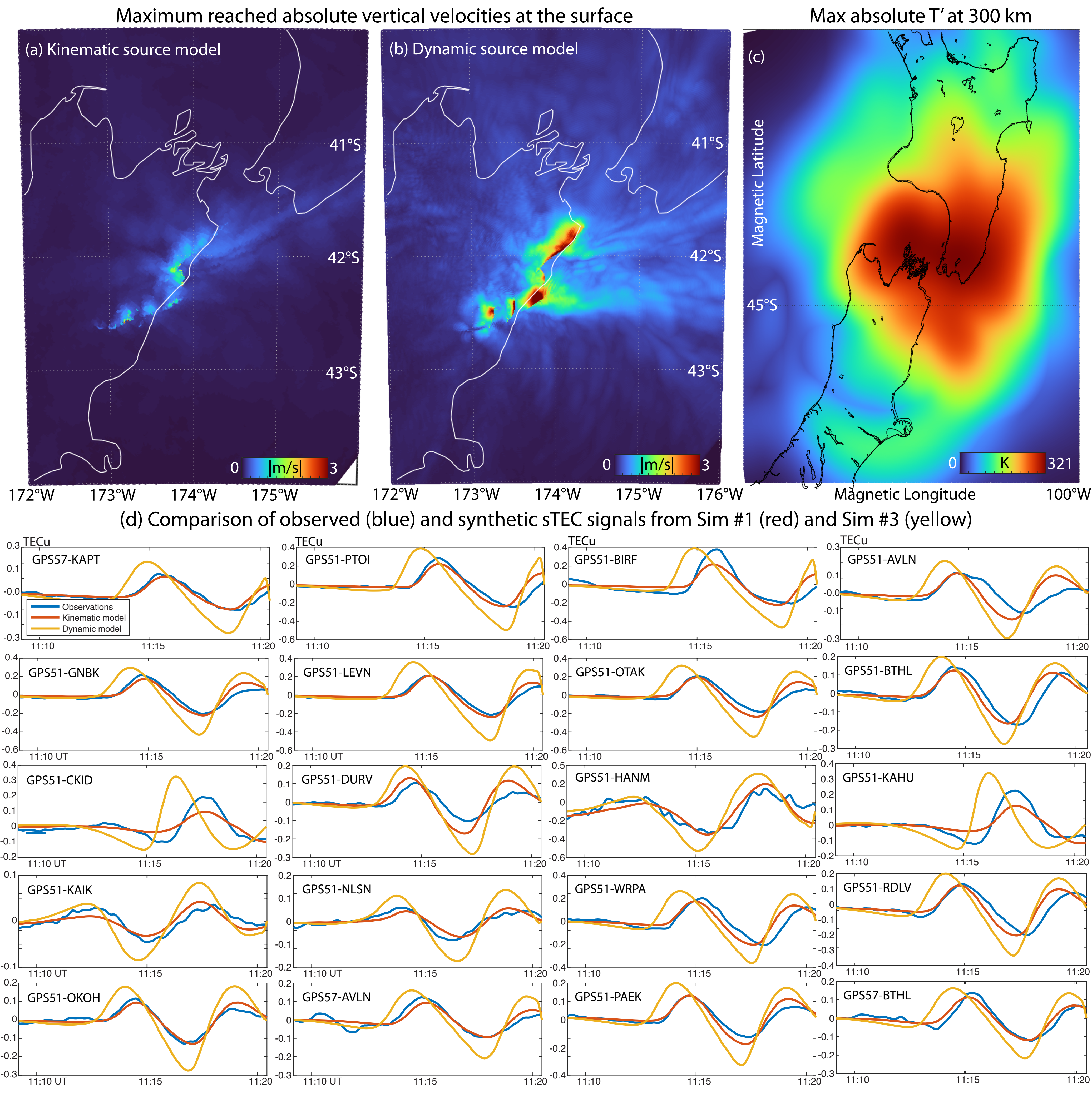

Maximum reached absolute vertical velocities at the surface
Max absolute T′ at 300 km
(a) Kinematic source model
(b) Dynamic source model
(c)
41°S
42°S
43°S
45°S
Magnetic Latitude
Magnetic Longitude
0
|m/s|
3
K
321
172°W
173°W
174°W
175°W
176°W
100°W
(d) Comparison of observed (blue) and synthetic sTEC signals from Sim #1 (red) and Sim #3 (yellow)
TECu
GPS57-KAPT
GPS51-PTOI
GPS51-BIRF
GPS51-AVLN
GPS51-GNBK
GPS51-LEVN
GPS51-OTAK
GPS51-BTHL
GPS51-CKID
GPS51-DURV
GPS51-HANM
GPS51-KAHU
GPS51-KAIK
GPS51-NLSN
GPS51-WRPA
GPS51-RDLV
GPS51-OKOH
GPS57-AVLN
GPS51-PAEK
GPS57-BTHL
Observations
Kinematic model
Dynamic model
11:10
11:10 UT
11:15
11:20